Nanoscale

ROYAL SOCIETY OF CHEMISTRY

PAPER

View Article Online
View Journal | View Issue

Cite this: *Nanoscale*, 2021, **13**, 7723

The in-plane structure domain size of nm-thick $MoSe_2$ uncovered by low-momentum phonon scattering

Huan Lin,†[a,b] Ridong Wang,†[c,b] Hamidreza Zobeiri,[b] Tianyu Wang,[d] Shen Xu*[e,b] and Xinwei Wang *[b]

Although 2D materials have been widely studied for more than a decade, very few studies have been reported on the in-plane structure domain (STD) size even though such a physical property is critical in determining the charge carrier and energy carrier transport. Grazing incidence X-ray diffraction (XRD) can be used for studying the in-plane structure of very thin samples, but it becomes more challenging to study few-layer 2D materials. In this work the nanosecond energy transport state-resolved Raman (nET-Raman) technique is applied to resolve this key problem by directly measuring the thermal reffusivity of 2D materials and determining the residual value at the 0 K-limit. Such a residual value is determined by low-momentum phonon scattering and can be directly used to characterize the in-plane STD size of 2D materials. Three suspended $MoSe_2$ (15, 50 and 62 nm thick) samples are measured using nET-Raman from room temperature down to 77 K. Based on low-momentum phonon scattering, the STD size is determined to be 58.7 nm and 84.5 nm for 50 nm and 62 nm thick samples, respectively. For comparison, the in-plane structure of bulk $MoSe_2$ that is used to prepare the measured nm-thick samples is characterized using XRD. It uncovers crystallite sizes of 64.8 nm in the (100) direction and 121 nm in the (010) direction. The STD size determined by our low momentum phonon scattering is close to the crystallite size determined by XRD, but still shows differences. The STD size by low-momentum phonon scattering is more affected by the crystallite sizes in all in-plane directions rather than that by XRD that is for a specific crystallographic orientation. Their close values demonstrate that during nanosheet preparation (peeling and transfer), the in-plane structure experiences very little damage.

Received 24th December 2020,
Accepted 22nd March 2021

DOI: 10.1039/d0nr09099a

rsc.li/nanoscale

1. Introduction

Graphene is one of the most widely used and attractive two-dimensional (2D) materials because of its fantastic properties. Owing to its feature of zero band gap, its applications in nanoelectronic devices such as field effect transistors (FET) are restricted.[1,2] As a family of novel 2D materials beyond graphene, transition metal dichalcogenides (TMDs) such as $MoSe_2$ and MoS_2 have been explored to make up for deficiencies in this area and also have attracted considerable interest.[3–5] Due to their ultrathin structure, there are many fantastic properties in 2D atomic layer materials, including $MoSe_2$, MoS_2 and graphene, which differ greatly from the properties of the corresponding bulk counterparts. Li *et al.* used scanning electron microscopy (SEM), Raman spectroscopy and transmission electron microscopy (TEM) to study the domain size of graphene films.[6] They found that graphene films grown on Cu were polycrystalline, with a domain area of tens of square micrometers. SEM and Raman spectroscopy clearly showed that the domains are increased by changing the growth parameters. Patil *et al.* synthesized $MoSe_2$ films by the chemical bath deposition method at room temperature (RT).[7] They characterized the structure of thin $MoSe_2$ films by X-ray diffraction (XRD) and SEM and the film was found to be polycrystalline in the hexagonal form. The grain sizes of the as-deposited $MoSe_2$ film are 22.4 nm and 22.1 nm uncovered by XRD and SEM. Hadland *et al.* used specular diffraction patterns and grazing-incidence X-ray diffraction (GIXRD) to determine the out-of-plane and in-plane structure of the $MoSe_2$ samples.[8] The results showed that the (hk0) planes rotate dis-

[a]*School of Environmental and Municipal Engineering, Qingdao University of Technology, Qingdao, Shandong, 266033, P. R. China*
[b]*Department of Mechanical Engineering, Iowa State University, Ames, IA 50011, USA. E-mail: shxu16@sues.edu.cn, xwang3@iastate.edu*
[c]*State Key Laboratory of Precision Measuring Technology and Instruments, Tianjin University, Tianjin, 300072, P. R. China*
[d]*Institute of Chemistry, Chinese Academy of Sciences, Beijing, 100190, P. R. China*
[e]*School of Mechanical and Automotive Engineering, Shanghai University of Engineering Science, Shanghai, 201620, P. R. China*
† Equal contribution authors.

orderly with each other, and all orientations are identically probable for large areas. In-plane diffraction revealed that the $MoSe_2$ gain size is on the order of 10–100 nm.

Although 2D materials have been widely studied for decades, very few studies have been reported on the structure domain size (STD size) in the in-plane direction even though such physical information is critical in determining the charge carrier and energy carrier transport. It is generally known that XRD spectroscopy can provide detailed information about the crystallite size of materials in a particular direction. The average crystallite thickness along a specific lattice plane direction can be obtained from each XRD peak. However, for extremely thin 2D materials (*e.g.* mono-layer samples), it is very difficult to obtain the STD size in the in-plane direction from XRD spectroscopy as the cross-section is extremely small and X-ray scattering is too weak to be detected. It should be pointed out that phonon scattering in thin 2D materials is strongly hindered by the STD size and could be used to characterize it. In addition, it is clear that the thermal transport of most kinds of 2D materials is dominated by the phonon–phonon scattering (Umklapp scattering) at near RT. Therefore, the Umklapp scattering is very strong and the structure domain boundary scattering could be relatively weak if the domain size is large. The grain boundary will have different scattering effects on phonons of different wavelengths and it is difficult to characterize the boundary scattering effect at moderate or high temperatures. Instead of XRD spectroscopy, the thermal reffusivity theory can be used to characterize the STD size by considering the phonon scattering in different lattice directions. At low temperatures, the mean free path of phonon–phonon scattering becomes very long due to the decrease of phonon density. Because when the temperature approaches absolute zero, all phonons are frozen, the phonon–phonon scattering is weakened. The only scattering source is structural scattering by grain boundaries, and surface and point defects and this structural scattering is independent of temperature. Therefore, the mean free path at extremely low temperatures can reflect the structural information about the $MoSe_2$ film. Wang's group first used the thermal reffusivity variation against temperature to determine the residual thermal reffusivity value at the 0 K limit and used this parameter to characterize the STD size of different materials.[9–15] Xu *et al.* for the first time used the thermal reffusivity theory to determine the phonon thermal resistivity of DNA.[9] Cheng *et al.* found that the STD size of an individual polycrystalline silver nanowire was 38.5 nm, which was larger than the value obtained from the XRD result [21 nm in the (311) direction].[10] In Xie *et al.*'s work, the STD size of the 3D graphene foam material was determined to be 166 nm, smaller than the crystallite size determined from the XRD result [201.8 nm corresponding to the (002) plane].[11] Xie *et al.* reviewed that the STD size of human hair (1.6 nm) agrees well with the crystallite size obtained from the XRD result (1.8 nm).[12] The thermal reffusivity theory has also been successfully used in investigating the STD size of other materials including ultrahigh molecular weight polyethylene (UHMWPE) fibers,[13] SiC microwires[14] and graphene paper (GP).[15] Liu *et al.* found that the STD size for the two UHMWPE fiber samples is 8.06 and 9.42 nm. They are smaller than the crystallite size determined by XRD [19.7 nm in the (002) direction].[13] Zhu *et al.* determined the STD size of three kinds of SiC microwires as 9.35, 1.42 and 1.03 nm, respectively, which are proportional to the corresponding crystalline size determined by XRD: 67–113, 14.6–18.4, and 5.85–7.84 nm.[14] Han *et al.* predicted a STD size of 375 nm for widely studied normal graphite materials, close to the 404 nm grain size uncovered by TEM. They also evaluated c-MFP induced by defect in the GP at 234 nm based on the thermal reffusivity theory.[15] Based on the above materials, the thermal reffusivity theory has been fully verified.

In this work, we measure the thermal diffusivity of thin $MoSe_2$ films (thickness from 15 nm to 62 nm) from RT down to 77 K using a novel nanosecond energy transport state-solved Raman (nET-Raman) technique. From thermal transport characterization we also obtain the thermal conductivity and optical properties of the $MoSe_2$ samples. Then the thermal reffusivity model is used to study the structural defect levels. The STD size from the thermal reffusivity model is very close to the result uncovered by XRD of bulk $MoSe_2$.

2. Experimental details

The nET-Raman technique is used to construct two distinct energy transport states in the time domain in order to measure the in-plane thermal diffusivity of suspended $MoSe_2$ films from RT down to 77 K. Continuous-wave (CW) and nanosecond (ns) lasers with 532 nm wavelength are used to irradiate the samples for both laser heating and Raman probing. The experimental setup and physical principle are shown in Fig. 1. As shown in Fig. 1(a), the sample is placed in an environment cell chamber which is supported on a 3D nanostage, so the sample can be moved precisely for laser spot positioning and focusing. The cell is filled with nitrogen gas and can be cooled down with liquid nitrogen. Inside the cell, the sample is placed on the heating/cooling block which can be heated with heating wire and cooled down with a cooling tube. The laser irradiated the center of the sample from the glass viewing window of the cell.

In the steady state, a CW laser (Excelsior, Spectra-Physics) is employed as the heating and probing source as shown in Fig. 1(b) and (d). During laser heating, Raman scattering induced by the heating laser could be collected and used to analyze the sample's thermal response. In the $MoSe_2$ sample, the heat generated from photon absorption will then propagate along its in-plane and out-of-plane directions. As the thickness of the sample is only a few to tens of nm, which is much smaller than its lateral size, it is reasonable to neglect the energy transfer and temperature distribution in the thickness direction. In this state, the temperature rise only depends on the in-plane thermal conductivity. By using different laser powers (P), we can use the Raman shift power coefficient (RSC), $\psi_{CW} = \partial\omega/\partial P = a{\cdot}\partial\omega/\partial T{\cdot}f_1(k)$, to describe the temperature

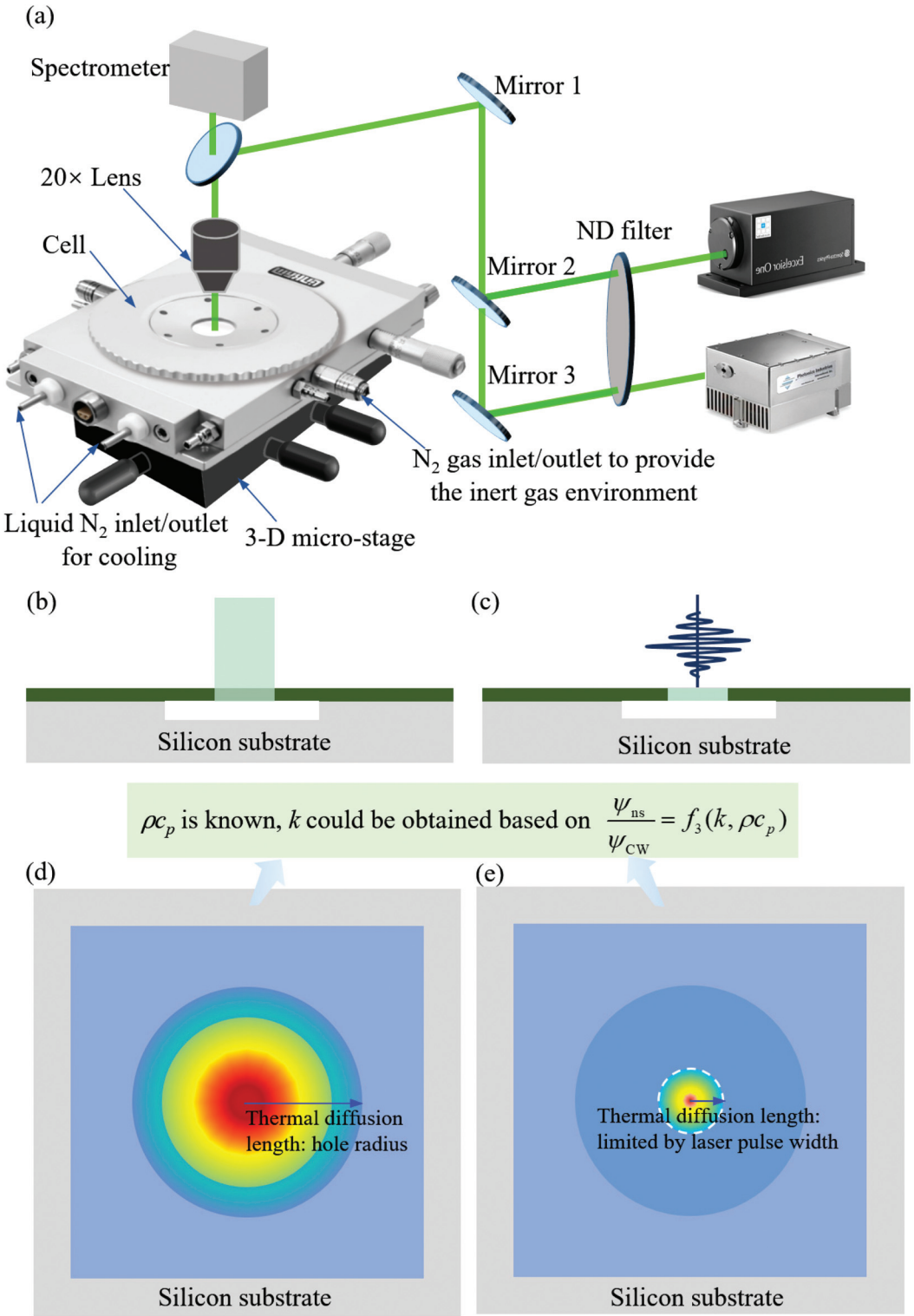

Fig. 1 (a) Schematic of the nET-Raman system. The environment cell is installed on a 3D nanostage. The cell chamber is filled with N_2 gas through the gas inlet/outlet. Liquid N_2 is used to cool down the chamber. (b)–(e) Two different energy transport states are generated by the 532 nm CW laser and 532 nm ns laser in the time domain with the same objective lens (20×). The in-plane thermal conductivity of the sample can be determined due to the different contributions of the in-plane thermal conductivity in the two energy transport states.

rise against the incident power. ψ_{CW} is dependent on the laser absorption coefficient (a), the temperature coefficient of Raman shift ($\partial\omega/\partial T$), and the in-plane thermal conductivity (k).

In the other energy transport state–transient energy transport state, a nanosecond (ns) laser (DCL AIO Laser, Photonics Industries, International, Inc.) is focused on the center of the same suspended sample. Fig. 1(c) illustrates that a ns laser is focused on the center of the suspended sample, which realizes local heating and transient Raman probing. Therefore, as shown in Fig. 1(e), in this transient state, the RSC has a different expression as $\psi_{ns} = \partial\omega/\partial P = a{\cdot}\partial\omega/\partial T{\cdot}f_2(k, \rho c_p)$. ψ_{ns} is dependent on the volumetric heat capacity (ρc_p) of the $MoSe_2$ sample besides the abovementioned properties including the laser absorption coefficient, the temperature coefficient of the Raman shift, and the in-plane thermal conductivity.

With the values of ψ_{CW} and ψ_{ns}, a normalized RSC can be determined as $\Theta = \psi_{ns}/\psi_{CW} = f_3(k, \rho c_p)$. In this way, the absorption coefficient and Raman temperature coefficient are eliminated. Assuming that the volumetric heat capacity of $MoSe_2$ has the same value as the bulk counterpart, the value of Θ only depends on the in-plane thermal conductivity of $MoSe_2$ films. Or if the specific heat is unknown, Θ will be determined by the sample's in-plane thermal diffusivity ($\alpha = k/\rho c_p$). Note that since the sample is very thin, the laser absorption depth (τ_L) value has negligible effect on the finally determined thermophysical properties.[16]

For the steady-state heating, the energy transport governing equation is:[17,18]

$$k\nabla^2 T_{CW} + \dot{q} = 0, \quad (1)$$

where T_{CW} is the temperature rise in the steady state, k (W m^{-1} K^{-1}) is the in-plane thermal conductivity, and $\dot{q}$ is volumetric Gaussian beam heating as shown below

$$\dot{q}(r,z) = (I_0/\tau_L)\exp(-r^2/{r_0}^2)\exp(-z/\tau_L), \quad (2)$$

where $I_0 = P/\pi{r_0}^2$ is the absorbed laser intensity in the center of the laser spot, τ_L is the laser absorption depth with $\tau_L = \lambda/(4\pi k_L)$,[19] in which λ is the laser wavelength (532 nm) and k_L is the extinction coefficient of the sample and r_0 is the characteristic radius of the laser spot. It should be pointed out that any deviation in k_L has negligible effect on our experiment result since the thickness is very small and the temperature is uniform in the thickness direction. Moreover, there is no laser absorption information needed in determining $\Theta = \psi_{ns}/\psi_{CW}$.

For transient-state heating, the pulse width of the nanosecond laser is 76 ns (full width at high maximum), and the interval between the two pulses is 10 μs. During the pulse heating, the diffusion length of $MoSe_2$ in the thickness direction is about 3 μm (ref. 20) which is much longer than the sample thickness (about 62 nm or less). Therefore, it is reasonable to assume that the sample has a uniform temperature distribution in the thickness direction. On the other hand, the time interval between two pulses (10 μs) is long enough for the $MoSe_2$ sample to cool down to the ambient temperature after a ns pulse heating. It is proved that there is no interference between ns pulses and no steady-state accumulated heat in the ns laser heating case. Therefore, the Fourier governing equation of nanosecond laser heating pulse can be written as:[21]

$$k\nabla^2 T_{ns} + \frac{I}{\tau_L} = \rho c_p \frac{\partial T_{ns}}{\partial t} \quad (3)$$

where T_{ns} is the transient temperature rise. The laser intensity I (W m^{-3}) is expressed by

$$I(r,z,t = I_0\exp(-r^2/{r_0}^2) \exp\left[-4\ln(2)t^2/{t_0}^2\right]\exp(z/\tau_L) \quad (4)$$

where I_0 (W m^{-2}) is the peak laser intensity, and t_0 (76 ns) is the pulse width of the ns laser.

The theoretical ratio of the temperature rise of the sample in the two states could be obtained by solving eqn (1) and (3), while the measured ratio is equal to the normalized RSC from the acquired Raman spectra. Through comparing the experimental normalized RSC with the theoretical ratio, we could determine the in-plane thermal conductivity of the sample based on the different contributions of heat conduction in these two energy transport states.

In order to determine the in-plane thermal conductivity of the $MoSe_2$ sample, a 3D heat conduction model is used to calculate the temperature rise in two energy transfer states. Through calculation, the theoretical relationship between the temperature rise ratio in the two cases and the in-plane thermal conductivity could be built. Finally, by varying the temperature of the environmental cell, the in-plane thermal conductivity of the samples against the temperature could be determined according to the measured Θ. More details on the simulation process are given in our previous work.[20] It needs to point out that during experiments, the measured Raman shift change in fact reflects the temperature rise that is a Raman intensity-weighted average over space for the CW case and over time and space for the ns laser case. Such physics is taken into full consideration in our computer modeling.[22]

3. Structure and morphology of nm-thick $MoSe_2$ samples

Three $MoSe_2$ samples are prepared by the mechanical exfoliation method from bulk $MoSe_2$ crystals. Using this method, we can obtain clean, highly crystalline and thin nanosheets of layered $MoSe_2$ samples.[23] These samples are slowly transferred to the circular hole on the center of a clean silicon substrate using two 3D nano stages. The diameter of the hole is 10 μm, and the depth is 3 μm. More details about sample preparation are given in the previous work of our group.[20]

Fig. 2(a)–(c) show the atomic force microscopy (AFM) images of three suspended $MoSe_2$ samples. In order to avoid sample damage of the suspended areas during AFM imaging, the thickness of the supported area near the suspended area is measured and used as the thickness of the sample. In Fig. 2

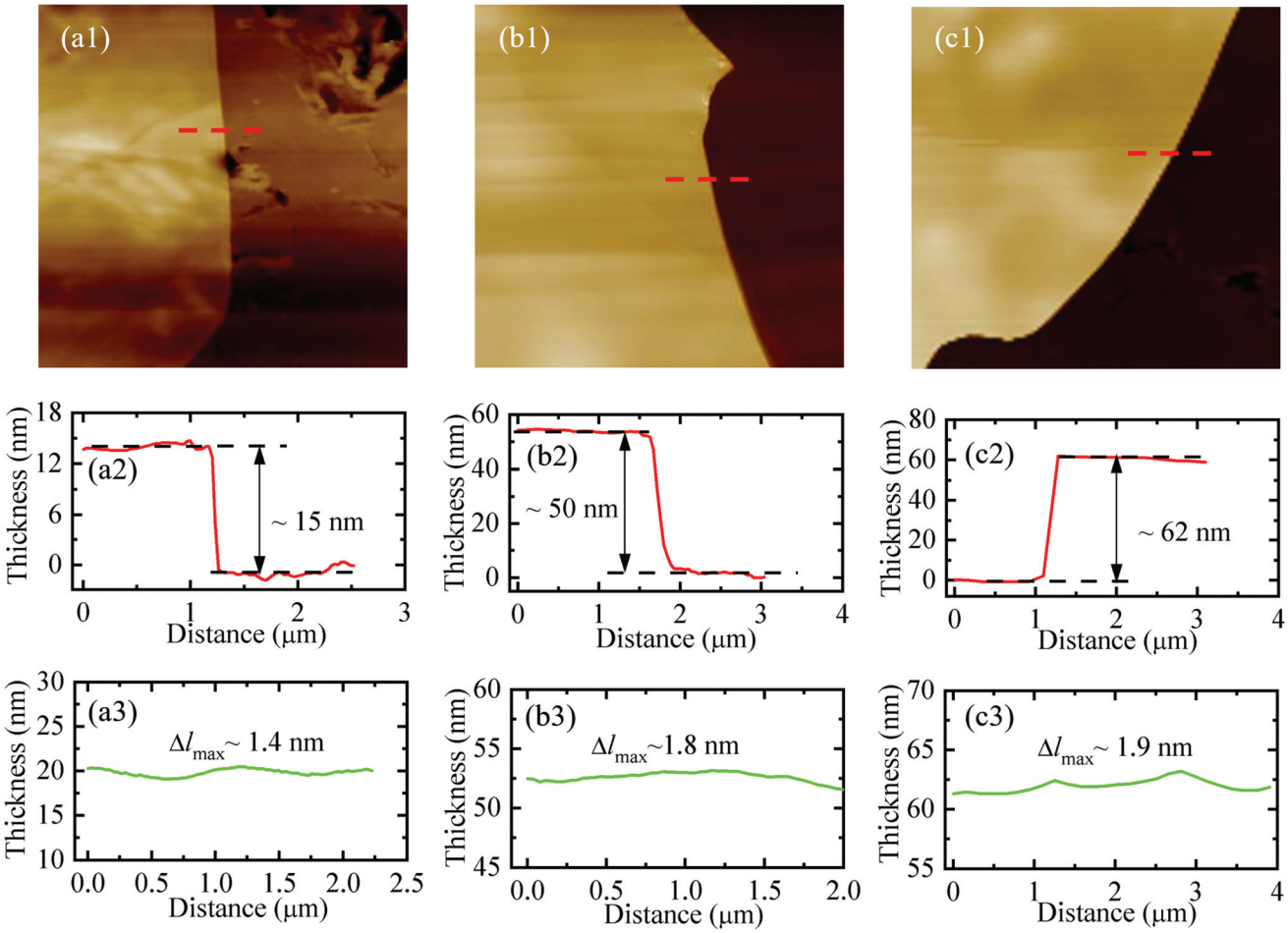

Fig. 2 AFM measurement results of three suspended $MoSe_2$ samples. (a1)–(c1) AFM images of three samples. (a2)–(c2) Thickness profiles corresponding to the red dashed line in figure (a1)–(c1). (a3)–(c3) Thickness profiles indicate the roughness of the measured area of three samples.

(a1)–(c1), the red dashed line represents the thickness profile shown in Fig. 2(a2)–(c2). The thickness of $MoSe_2$ samples is 15, 50 and 62 nm, respectively. The surface roughness is then expressed by the maximum thickness variation (Δl_{max}) along a line on the sample surface. As shown in Fig. 2(a3)–(c3), the values of $\Delta l_{max}$of these samples are relatively small compared with the thickness of the samples. When the thickness increases, Δl_{max}also increases a little bit.

4. Thermal diffusivity, conductivity, and structure domain

4.1 Thermal diffusivity determined using nET-Raman

In the Raman experiments, the Raman spectra from RT to 77 K are collected automatically for all samples under different laser powers to obtain the RSC. Both the CW and ns laser powers are adjusted to achieve a suitable but low temperature rise on the sample in order to avoid sample damage and to remain within the linear temperature correlation of the Raman shift. Taking the 50 nm thick sample as an example, the CW laser power is from 0.75 mW to 2.97 mW at 77 K under 20× objective lens, and the ns laser power varies from 0.19 mW to 0.48 mW at 77 K under 20× objective lens. For the 15 nm thick sample, at low temperatures, the Raman signal is not very good. The sample's thermal resistance is proportional to the inverse of its thickness. For the 15 nm thick sample to reach the same level temperature rise of thicker samples, it needs much less laser absorption. In fact, the needed laser absorption is proportional to its thickness. This will significantly reduce the Raman signal, making it have very large uncertainties. The femtosecond stimulated Raman spectroscopy technique[24,25] can improve the signal for extremely thin 2D materials at low temperatures. Here, we only conduct the nET-Raman experiment at RT for it. Therefore, the laser powers of the 15 nm thick sample at 296 K, and 50 nm and 62 nm thick samples at 77 K are summarized in Table 1. In this work, the selection of a large laser spot under the 20× objective is for minimizing the hot carrier diffusion effect to a negligible level.[16] The hot carrier diffusion length is estimated as $L_c = \sqrt{\tau D}$, where τ is the lifetime of hot carriers and D is the hot carrier diffusivity. Since τ is on the order of 100 ps (ref. 26 and 27) and $D \sim 10^{-4}$ m^2 s^{-1},[28] the hot carrier diffusion length is in the order of 100 nm. Since this diffusion length is much

Table 1 Summary of the CW and ns laser power ranges and the corresponding laser spot diameters (20×)

Sample thickness (nm)	Temperature (K)	CW laser power range (mW)	ns laser power range (mW)	CW laser spot diameter (μm)	ns laser spot diameter (μm)
15	296	0.15–0.62	0.01–0.04	2.967	2.412
50	77	0.75–2.97	0.19–0.48	3.030	2.175
62	77	0.82–3.25	0.37–0.95	3.268	2.071

shorter than the laser spot size under 20× objective lens for suspended samples, the effect of hot carrier diffusion becomes negligible. Also at each temperature, the laser spot size is measured *in situ* and used in thermal transport modeling for data processing. The diameters of the two laser spots on different samples are measured and also listed in Table 1.

Fig. 3(a) and (b) show the contour plots of the Raman peak at ~240 cm^{-1} under varied powers of the two different lasers, indicating that the peak is redshifted with the increased laser power. This concludes that the local temperature of the sample increases with the increased laser power. It can be seen in Fig. 3(c) and (d) that the measured Raman shift of the A_{1g} peak (~240 cm^{-1}) is almost linearly related to the laser power. Accordingly, the A_{1g} peak of $MoSe_2$ is used to determine the RSC value in this work. The linearly fitted slope, RSC of the A_{1g} mode, is -0.345 ± 0.002 cm^{-1} mW^{-1} under a CW laser, and -2.318 ± 0.103 cm^{-1} mW^{-1} under a ns laser. The corresponding normalized RSC (Θ) is 6.72 ± 0.31. Fig. 3(e) shows the theoretical Θ curve of the 50 nm thick sample at 77 K, 225 K and 296 K. The value obtained in the experiments is used to interpolate the theoretical result to determine the thermal diffusivity. Taking the 50 nm thick $MoSe_2$ at 77 K for example, the thermal diffusivity is determined as $(1.52 \pm 0.14) \times 10^{-5}$ m^2 s^{-1} as shown in the figure.

The measured thermal diffusivity for the 50 nm thick $MoSe_2$ layer from RT to 77 K is presented in Fig. 3(f). As the temperature goes down, α increases slowly. The variation trend of thermal diffusivity with temperature will be explained later according to the concept of thermal reffusivity. The experimental result of the specific heat[29] of $MoSe_2$ is plotted in Fig. 3(f). Its density is 6900 kg m^{-3}.[30] Using the specific heat and density of $MoSe_2$, the thermal conductivity k_{nET} (determined using this nET-Raman) of $MoSe_2$ is calculated and the results are shown in Fig. 3(f). k_{nET} increases from 9.19 to 15.07 W m^{-1} K^{-1} from RT to 100 K, and drops to 12.24 W m^{-1} K^{-1} at 77 K. It should be pointed out that the temperature rise of the 50 nm thick sample under laser irradiation is less than 30 K. It can be seen from Fig. 3(c) that the change of Raman shift is about 0.7 cm^{-1} in the CW case. The average temperature coefficient of the Raman shift ($\partial\omega/\partial T$) is around 0.008 cm^{-1} K^{-1} as shown in Fig. 4(b). Therefore, we can calculate the temperature rise of the sample under a CW laser spot as $\Delta T = \Delta\omega/(\partial\omega/\partial T)$ = 88 K. The average temperature rise of the entire sample in all domains is about 29 K.[22] The average temperature rise of the entire sample in all domains under a ns laser is less than 29 K as the laser heating time is very short and the sample experiences a transient process. Our measurement data agree well with those published using other Raman techniques. Differences are largely due to the sample-to-sample structure variation and experimental control deviations. For instance, Wang *et al.* measured the thermal conductivity of suspended $MoSe_2$ increasing from 11.1 ± 0.4 to 20.3 ± 0.9 W m^{-1} K^{-1} with the increased thickness (45 nm to 140 nm) at RT.[20] Zobeiri *et al.* measured the in-plane thermal conductivity of these films increased from 6.2 ± 0.9 to 25.7 ± 7.7 W m^{-1} K^{-1} when the sample thickness varied from 5 to 80 nm using frequency-domain energy transport state-resolved Raman (FET-Raman) technique.[22] The reduction in the thermal conductivity is due to the enhancement of the phonon scattering effect on the surface of thinner samples. Using the optothermal Raman technique, Zhang *et al.* found that the room-temperature thermal conductivities are 59 ± 18 W m^{-1} K^{-1} and 43 ± 12 W m^{-1} K^{-1} for single-layer and bi-layer $MoSe_2$, respectively.[31] Due to the phonon–phonon scattering, the thermal conductivities decrease when supported on a substrate and decrease with the increased temperature. Gu *et al.* estimated that the phononic thermal conductivity of single-layer $MoSe_2$ is 54 W m^{-1} K^{-1} using the first-principles-based PBTE approach.[32]

4.2 Benchmark of the observed thermal conductivity variation with temperature

In traditional steady state Raman based thermal characterization, the laser absorption needs to be precisely determined in order to evaluate the thermal conductivity and interface thermal conductance of 2D materials, and this could bring in significant measurement uncertainties. Here by analyzing the CW case, we intend to demonstrate that laser absorption in suspended 2D materials can significantly differ from that by theoretical calculations. In the steady state, the Raman shift *versus* temperature for the 50 nm thick sample at the same excitation laser power under 20× laser objective lens is first measured and shown in Fig. 4(a) and (b). It is noted that the Raman peak blue shifts when the temperature decreases from RT to about 77 K. The $\omega \sim T$ relation is fitted using a polynomial function as $\omega = 243.8296 - 4.59 \times 10^{-3}T - 8.76758 \times 10^{-6}T^2$. Using different laser powers (P), we obtain the RSC in the steady state which can be expressed as $\partial\omega/\partial P$ and the result is shown in Fig. 4(d) for each environment temperature point. During laser heating, the temperature rise in the sample is $\Delta T = (\Delta P \times f)/k_{CW}$, where f is a constant value and k_{CW} is the thermal conductivity of the sample under steady state heating. As we know, $\Delta\omega = (\partial\omega/\partial T) \times \Delta T$, combining with the expression of ΔT, we can get $\Delta\omega/\Delta P = (1/k_{CW})\cdot\partial\omega/\partial T\cdot f$, where $\partial\omega/\partial T$ is the temperature coefficient of the Raman shift. At RT, if we use the

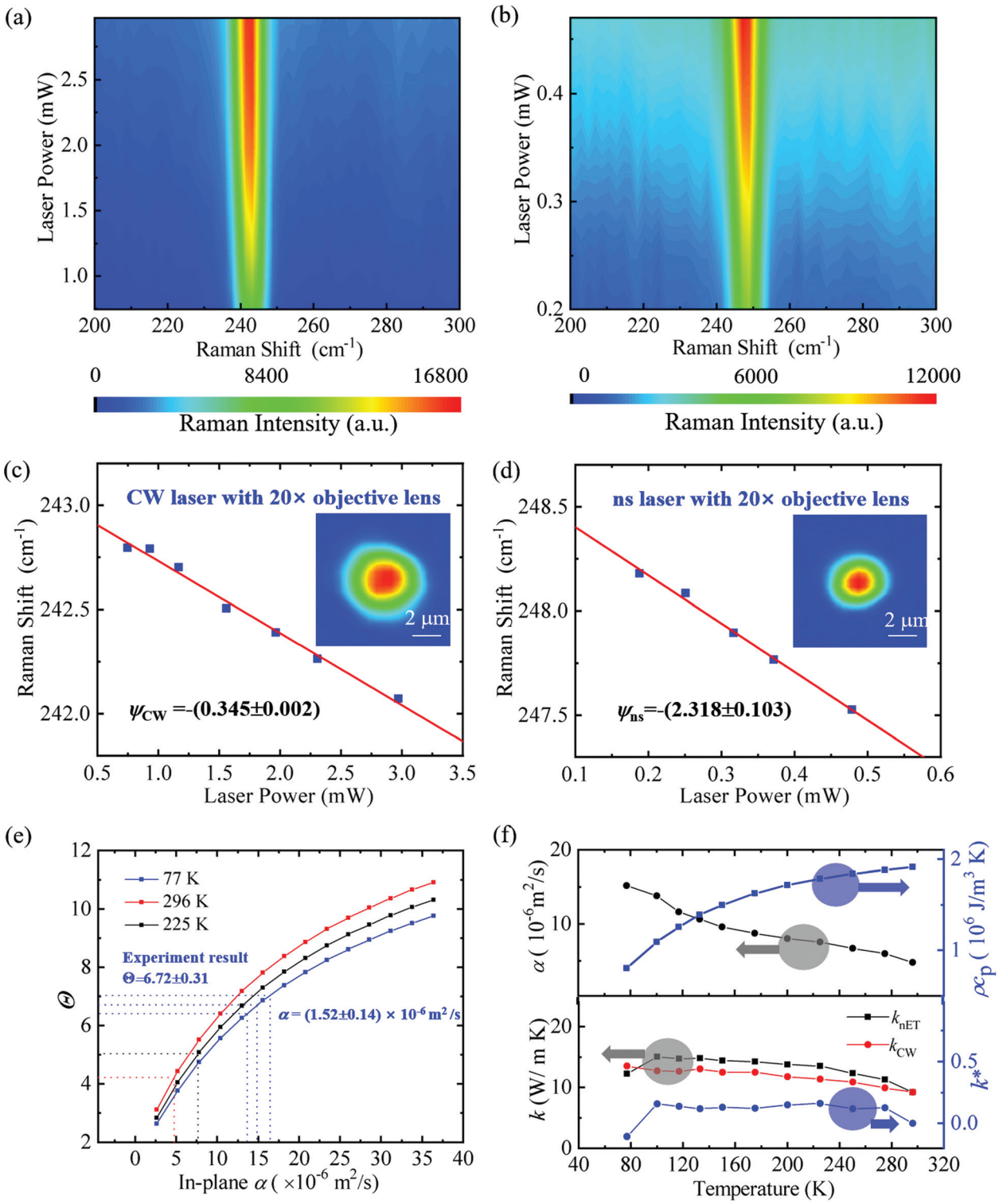

Fig. 3 The 50 nm-thick sample at 77 K is used to illustrate the results of the nET-Raman experiment. (a) and (b) 2D contour plots to demonstrate the variation of the Raman spectrum with laser power of (a) CW laser and (b) ns laser. (c) and (d) The Raman wavenumber shift with laser power for CW and ns lasers. The solid lines in the figures are the linear fitting result for Raman power coefficient. The insets are the spots of two lasers. (e) Data fittings of experimental Θ against that obtained by 3D numerical modeling to determine the thermal diffusivity. These are for the 50 nm thick $MoSe_2$ sample at 77 K, 225 K and 296 K. (f) The measured thermal diffusivity, specific heat of $MoSe_2$ from the literature[29] and calculated thermal conductivity of 50 nm-thick $MoSe_2$.

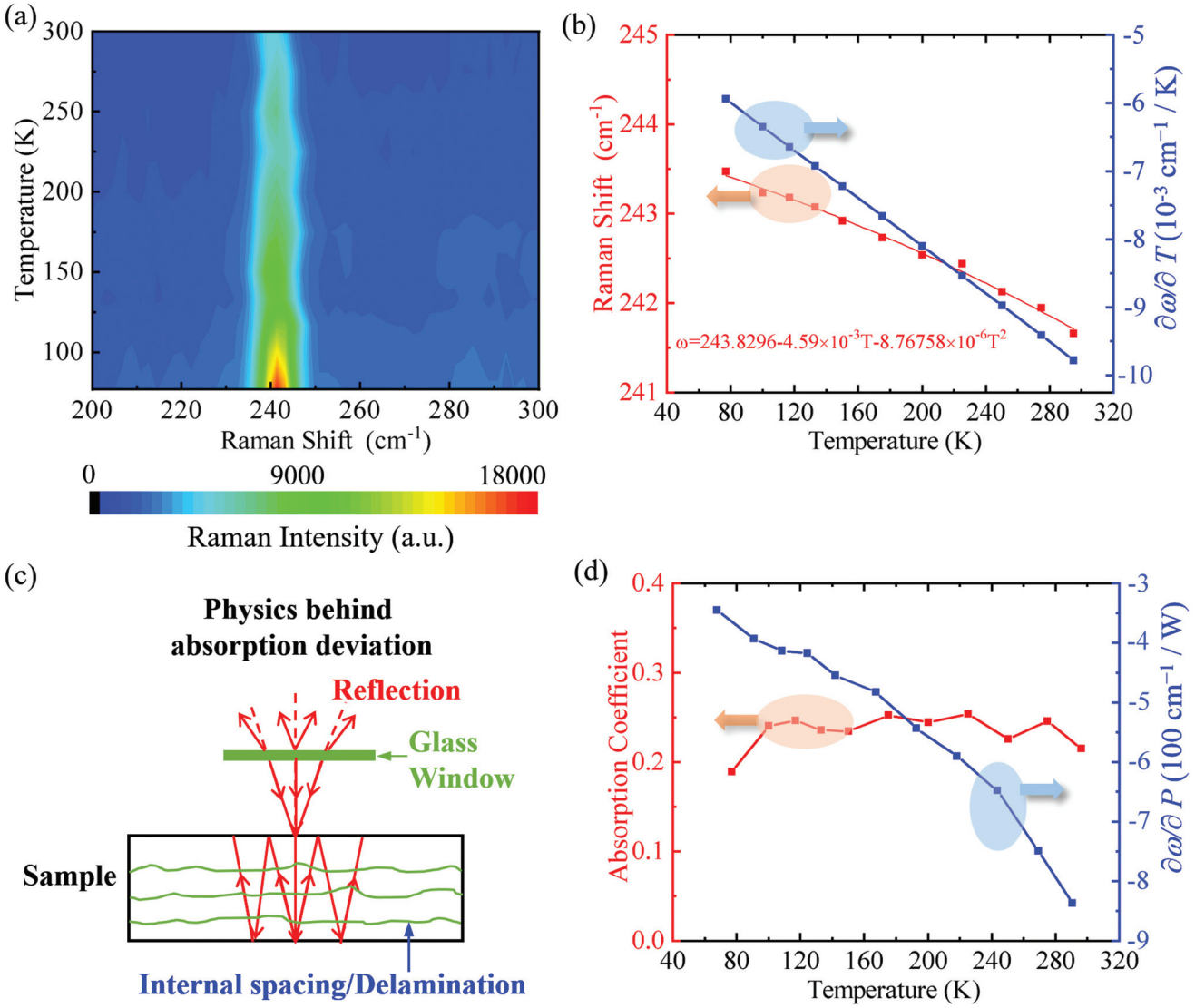

Fig. 4 (a) The 2D contour maps to demonstrate the variation of the Raman shift against the temperature of 50 nm thick $MoSe_2$ at the same excitation laser power under 20× laser objective lens with a CW laser. (b) The Raman shift and the temperature coefficient of the Raman shift ($\partial\omega/\partial T$) *versus* temperature for the 50 nm-thick sample. (c) Physics behind absorption deviation. The presence of spacing between $MoSe_2$ layers can greatly alter the absorption behavior. (d) The Raman shift power coefficient (RSC) and absorption coefficient *versus* temperature for the 50 nm thick sample.

value of k_{nET} as the value of k_{CW}, f can be obtained. k_{CW} at other temperatures is then calculated by utilizing the relation of $k_{CW} = \partial\omega/\partial T{\cdot}\partial\omega/\partial P{\cdot}f$, and the results are shown in Fig. 3(f). It is clear in Fig. 3(f) that from RT to 100 K, k_{nET} increases from 9.19 to 15.07 W m^{-1} K^{-1} at 77 K, and it drops to 12.24 W m^{-1} K^{-1}. For k_{CW}, it increases slowly from 9.19 to 13.55 W m^{-1} K^{-1}. The relative difference between k_{nET} and k_{CW} [$k^* = (k_{nET} - k_{CW})/k_{nET}$] is around −11% to 16% [shown in Fig. 3(f)]. There are some differences between k_{nET} and k_{CW} values. One major possible reason is the optical property change with temperature which could change the laser absorption in the sample. But still these two methods give very close results with a difference less than 16%. This also confirms the data accuracy measured by the nET-Raman technique. Below we analyze the data in a different aspect to identify the laser absorption coefficient based on k_{nET}, $\partial\omega/\partial P$, and $\partial\omega/\partial T$ for the CW case.

Here we also take the 50 nm thick sample for example to illustrate the results. Fig. 4(b) and (d) show the temperature coefficient of the Raman shift ($\partial\omega/\partial T$) and the RSC ($\partial\omega/\partial P$) against temperature. As we know, $(\partial\omega/\partial P)/(\partial\omega/\partial T) = \partial T/\partial P = \Delta T_1$, which is the temperature rise in the sample under unit laser energy irradiation. From simulation, a temperature rise ΔT_0 in each case can also be obtained considering the laser spot size and thermal conductivity k_{nET}. In this way, the laser absorption coefficient a can be determined as $a = \Delta T_1[1 - \exp(-\Delta z/\tau_L)]/\Delta T_0$, in which $\tau_L = \lambda/(4\pi k_L)$[19] is the laser absorption depth of $MoSe_2$, λ is the laser wavelength of 532 nm, and k_L is

the extinction coefficient. The term $[1 - \exp(-\Delta z/\tau_L)]$ is the laser absorption used in the modeling. When λ is 532 nm, the refractive index and extinction coefficient of $MoSe_2$ are 4.8 and 2.08,[33] respectively, and we have τ_L = 20.4 nm. In this way, the calculated values of a are all around 0.25 as shown in Fig. 4(d).

The multiple reflection of the incident laser beam in a suspended film will enhance the absorption of the incident laser by the film, which has been studied in the previous work.[34,35] Inspired by these references, we calculate the theoretical a to be 0.52 with rigorous consideration of the multi-reflection and interference within the 50 nm thick sample. The theoretical laser absorption coefficient is about twice that obtained from the experiment. We speculate that there are several factors accounting for this difference. First, in the studies reported by other researchers, the laser beam absorption was evaluated based on the refractive index of n = 4.8 (ref. 33) for $MoSe_2$. However, this optical property varies in a large range due to the differences among the measured samples. For instance, from ref. 36 and 37, they found that the refractive index and extinction coefficient of $MoSe_2$ are 2.25, 0.75 and 4.22, 1.61 at 532 nm. Second, our samples are housed in a cryogenic environment cell with a layer of glass on top of it. The laser irritates the sample after going through the glass as shown in Fig. 4(c), and the calculated reflectivity of glass is 6% when the laser is perpendicular to the surface of the sample. Additionally, the laser beam is focused with a limited numerical aperture. The reflectivity of glass for this converged laser beam will be higher than 6% which could bring in large errors in laser absorption calculation. Last but not least, the spacing between $MoSe_2$ layers within the sample might be increased (due to delamination) during the sample preparation. The presence of spacing, although tiny ones, can greatly alter the absorption behavior. Our finding also raises a critical point: it is extremely challenging and difficult to determine the precise laser absorption in 2D materials' thermal characterization. Instead, the nET-Raman technique completely eliminates this problem and determines the thermophysical properties of 2D materials with unprecedented accuracy.

4.3 Structure domain size determined by low-momentum phonon scattering

In the thermal reffusivity model, the in-plane thermal reffusivity (Θ_t) is defined as the inverse of the thermal diffusivity for the measured $MoSe_2$. For metals and the cross-plane direction of 2D materials, the definition of the thermal reffusivity will have to be modified to consider the intrinsic specific heat of energy carriers.[10,39] Here, the thermal reffusivity is correlated with the phonon population and scattering behavior and is expressed as:[40]

$$\Theta_t = \Theta_0 + C \times e^{-\theta/2T}, \quad (5)$$

It is clear that the thermal reffusivity drops when the temperature decreases and finally reaches a constant value (Θ_0) at the 0 K limit. C is a constant, and Θ_0 is termed the residual thermal reffusivity and describes the influence of defect scattering only. θ is a constant proportional to Debye temperature. By fitting the thermal reffusivity against temperature data using the thermal reffusivity model, the Θ_0 value and structure domain size can be extracted. Taking the 62 nm thick sample for example, the results are shown in Fig. 5(a). The fitting curves by the thermal reffusivity model are also given in the figure, which provides a good fitting of the experimental data. From the fitting result, we have $\Theta_t = 5.10 \times 10^4 + 4.46 \times 10^5 \times e^{-234/T}$, and the Θ_0 value is 5.10×10^4 s m^{-2}. To avoid damaging the 15 nm thick sample, we only conduct the nET-Raman experiment at RT since its Raman signal is not very good at low temperatures under ns laser heating. At other temperatures, CW Raman is used to obtain k_{CW} from the relation of $k_{CW} = \partial\omega/\partial T \cdot \partial\omega/\partial P \cdot f$. As shown in Fig. 5(a), the thermal reffusivity of the 15 nm thick sample has large variations, mostly due to the large uncertainties in its weak Raman signal. However, the residual thermal reffusivity can still be determined based on the data trend, which is quite close to that of the 62 nm-thick sample.

There are three kinds of acoustic phonon modes: longitudinal acoustic (LA), flexural acoustic (ZA), and transverse acoustic (TA) mode. In the LA mode, the atomic displacements are along the wave propagation direction. In the TA mode, the in-plane displacements are perpendicular to the propagation direction, and the ZA mode corresponds to out-of-plane atomic displacements. The phonon dispersion gives the relationship between the phonon wave vector q and the phonon energy E or frequency ω ($E = \hbar\omega$ where $\hbar$ is the reduced Planck constant). At the 0 K-limit, the phonon momentum goes to zero, which corresponds to the low phonon wave vector q near the center of the Brillouin zone. At this location, the frequency of the LA and TA modes has approximately linear dispersions[41,42] as $\omega_{LA} \approx v_{LA}q$ and $\omega_{TA} \approx v_{TA}q$, respectively. The phonon group velocity is $v = d\omega/dq$. Therefore, the velocities v_{LA}, v_{TA} and v_{ZA} are the slopes of each dispersion curve at point Γ(0,0,0) in Fig. 5(c), which are 799, 313, and 494 m s^{-1}, respectively. From the equation $v^{-1} = 1/3 (v_{LA}{}^{-1} + v_{TA}{}^{-1} + v_{ZA}{}^{-1})$, the average phonon velocity v can be calculated as 464 m s^{-1}. For the in-plane thermal reffusivity, we have $\Theta_0 = 2/(vl_0)$. Θ_0 is found to be 7.34×10^4 s m^{-2} for the 50 nm-thick sample, so the STD size l_0 is determined to be 58.7 nm. Using the same procedure, the STD size for the 62 nm thick sample is calculated to be 84.5 nm.

To further understand the in-plane STD size, XRD is used to characterize the structure of $MoSe_2$ bulk and the XRD pattern is shown in Fig. 5(b). The sharp peaks reveal the polycrystallinity of the $MoSe_2$ bulk that is used to prepare the nanosheets. This is analyzed to determine the crystal structure of $MoSe_2$. The observed interplane distance d values are used to determine the crystal structure. The $MoSe_2$ bulk shows prominent (002), (004), (006), (008), (100), (110) and (010) peaks. The crystallite size in each direction is calculated using the Scherrer formula and the results are shown in Fig. 5(b). Specifically, for the in-plane direction, the crystallite size is determined to be 64.8 nm for

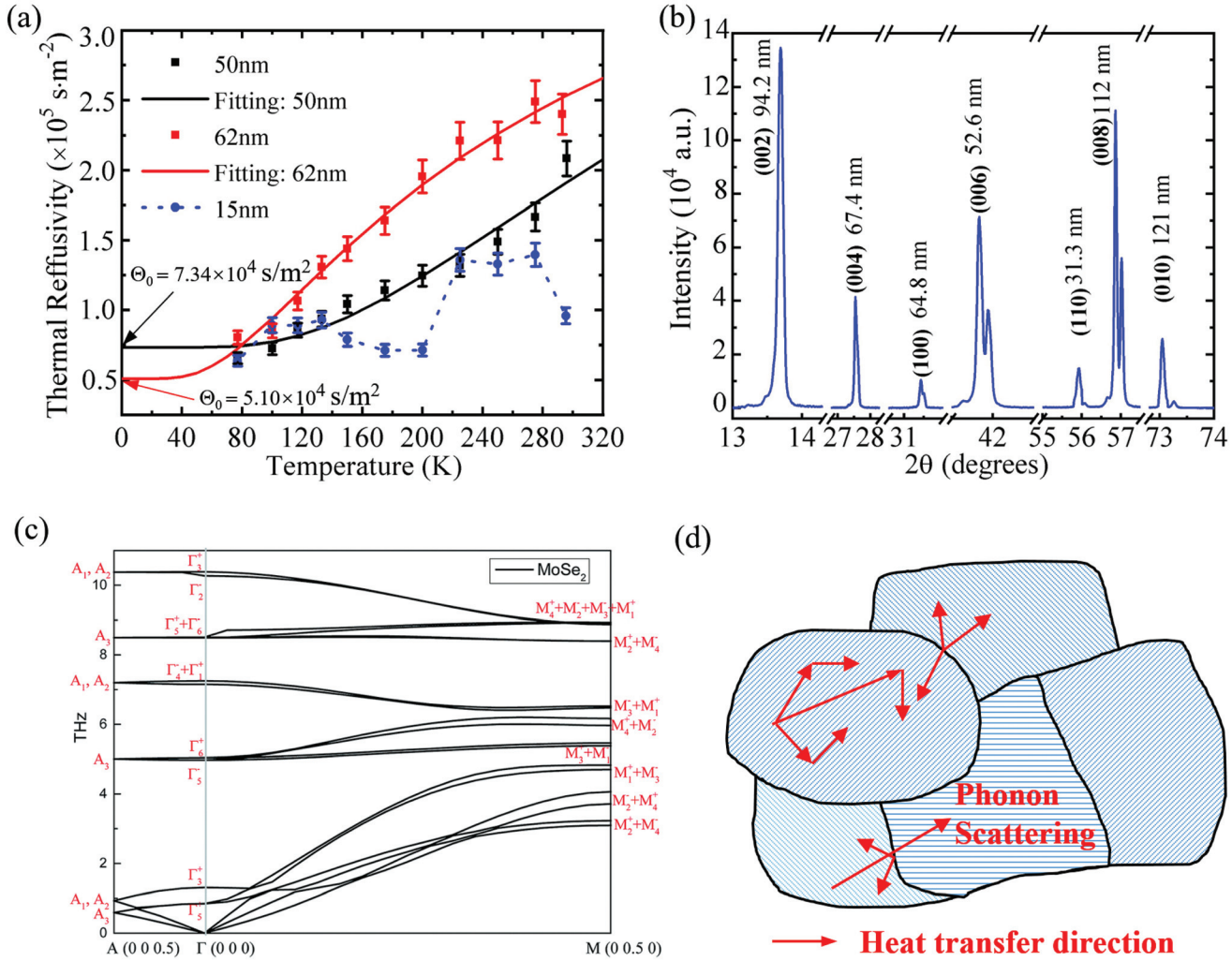

Fig. 5 (a) Variation of the thermal reffusivity with temperature for the three samples. The residual thermal reffusivities for 62 nm-thick and 50 nm-thick samples are determined to be 5.10 × 10^4 and 7.34 × 10^4 s m^{-2}, respectively. This is caused by the defects in the films. (b) XRD pattern of bulk $MoSe_2$. According to the XRD results, the crystallite sizes determined by the peaks (002), (004) (006), (008), (100), (110) and (010) are 94.2 nm, 67.4 nm, 64.8 nm, 52.6 nm, 31.3 nm, 112 nm and 121 nm, respectively. (c) The phonon dispersion relationship and irreducible representations of phonon modes at A, G and M points are shown for $MoSe_2$. Note that the path Γ–A refers to the [001] direction, and Γ–M is parallel to the [010] direction[38] (reproduced from ref. 38 with permission from The Royal Society of Chemistry). (d) Phonon scattering in the in-plane direction. The arrows indicate the direction of phonon scattering and propagation.

(100), 31.3 nm for (110), and 121 nm for (010) direction. In the out-of-plane directions, the crystallite size is 94.2 nm for (002), 67.4 nm for (004), 52.6 nm for (006), and 112 nm for the (008) direction. These similar crystallite sizes determined from different peaks indicate that the crystallite in $MoSe_2$ is sphere-like. Compared with the value of 64.8 nm [(100) plane] characterized by XRD, the STD size determined by low-momentum phonon scattering is very close, but still shows some differences. XRD can be used for providing detailed information about the crystallite size and structural order of materials in a specified direction. The average crystallite thickness along a specific lattice plane is obtained from each XRD peak. However, the thermal reffusivity model characterizes the STD size by considering the phonon scattering from all the lattice directions. Therefore, the STD size given by the thermal reffusivity model is actually the effective domain size with a combined microcrystalline effect from every in-plane direction as shown in Fig. 5(d). So, deviation could arise when compared with those by XRD. Theoretically, the grain sizes in different crystallographical directions can be obtained from the TEM results. However, TEM is rarely used in 2D material crystallite size characterization. The main reason is that the preparation of the sample is very difficult. Additionally, the sample will suffer from additional damage in the process of transfer and the anticipated information cannot be obtained. However, the STD size determined by low-momentum phonon scattering is very close to the in-plane crystallite size of bulk $MoSe_2$. This indicates that during our nm-thick $MoSe_2$ preparation, the sample experiences very little in-plane structure damage.

5. Conclusions

In this work, three suspended nm-thick $MoSe_2$ samples were measured using the nET-Raman technique at different temperatures (RT down to 77 K) for structure domain exploration. nET-Raman used a continuous wave laser and a nanosecond laser to heat the material and simultaneously excite Raman signals. In these two energy transport states, the Raman-shift power coefficients of the two states were measured, and the in-plane thermal diffusivity was determined using their ratio. Using the thermal reffusivity theory, the 0 K-limit residual thermal reffusivity was determined to be 7.34×10^4 and 5.10×10^4 s m^{-2} for the 50 nm and 62 nm thick samples, respectively. These finite values reflect the existence of defects in the samples. The corresponding structure domain size was determined to be 58.7 nm and 84.5 nm for the 50 nm and 62 nm thick samples, respectively, based on the residual thermal reffusivity that reflects the low-momentum phonon scattering. For the in-plane direction structure, our XRD study uncovered crystallite sizes of 64.8 nm in the (100) direction and 121 nm in the (010) direction for bulk $MoSe_2$ that the nanosheets were peeled off from. The STD size determined by low momentum phonon scattering is more affected by the crystallite size in all in-plane directions different from that of XRD that is for a specific crystallographic orientation. The close value of STD size determined by low momentum phonon scattering compared with that of bulk $MoSe_2$ determined by XRD confirms that during nanosheet preparation (peeling and transfer), the in-plane structure experienced very little damage.

Conflicts of interest

There are no conflicts to declare.

Acknowledgements

This work was supported by the US National Science Foundation (CBET1930866 and CMMI2032464 for X. W.), the National Key Research and Development Program (2019YFE0119900 for H. L.), the National Natural Science Foundation of China (52005367 for R. W.), and the Natural Science Foundation of Shandong Province (ZR2020ME183 for H. L.). Huan Lin and Shen Xu are grateful to the China Scholarship Council. Shen Xu is grateful to the research supported by the Program for Professor of Special Appointment (Eastern Scholar) at Shanghai Institutions of Higher Learning.

References

1 S. J. Zhang, S. S. Lin, X. Q. Li, X. Y. Liu, H. A. Wu, W. L. Xu, P. Wang, Z. Q. Wu, H. K. Zhong and Z. J. Xu, *Nanoscale*, 2016, **8**, 226–232.
2 T. Shimizu, J. Haruyama, D. C. Marcano, D. V. Kosinkin, J. M. Tour, K. Hirose and K. Suenaga, *Nat. Nanotechnol.*, 2011, **6**, 45–50.
3 Q. H. Wang, K. Kalantar-Zadeh, A. Kis, J. N. Coleman and M. S. Strano, *Nat. Nanotechnol.*, 2012, **7**, 699.
4 S. Tongay, J. Zhou, C. Ataca, K. Lo, T. S. Matthews, J. Li, J. C. Grossman and J. Q. Wu, *Nano Lett.*, 2012, **12**, 5576–5580.
5 Z. Ahmadi, B. Yakupoglu, N. Azam, S. Elafandi and M. Mahjouri-Samani, *Int. J. Extreme Manuf.*, 2019, **1**, 015001.
6 X. Li, C. W. Magnuson, A. Venugopal, J. An, J. W. Suk, B. Han, M. Borysiak, W. Cai, A. Velamakanni and Y. Zhu, *Nano Lett.*, 2010, **10**, 4328–4334.
7 P. P. Hankare, A. A. Patil, P. A. Chate, K. M. Garadkar, D. J. Sathe, A. H. Manikshete and I. S. Mulla, *J. Cryst. Growth*, 2008, **311**, 15–19.
8 E. C. Hadland, H. Jang, N. Wolff, R. Fischer, A. C. Lygo, G. Mitchson, D. Li, L. Kienle, D. G. Cahill and D. C. Johnson, *Nanotechnology*, 2019, **30**, 285401.
9 Z. Xu, X. Wang and H. Xie, *Polymer*, 2014, **55**, 6373–6380.
10 Z. Cheng, L. Liu, S. Xu, M. Lu and X. Wang, *Sci. Rep.*, 2015, **5**, 10718.
11 Y. Xie, Z. Xu, S. Xu, Z. Cheng, N. Hashemi, C. Deng and X. Wang, *Nanoscale*, 2015, **7**, 10101–10110.
12 Y. Xie, B. Zhu, J. Liu, Z. Xu and X. Wang, *Front. Energy*, 2018, 1–15.
13 J. Liu, Z. Xu, Z. Cheng, S. Xu and X. Wang, *ACS Appl. Mater. Interfaces*, 2015, **7**, 27279–27288.
14 B. Zhu, R. Wang, S. Harrison, K. Williams, R. Goduguchinta, J. Schneiter, J. Pegna, E. Vaaler and X. Wang, *Ceram. Int.*, 2018, **44**, 11218–11224.
15 M. Han, J. Liu, Y. Xie and X. Wang, *Carbon*, 2018, **126**, 532–543.
16 H. Zobeiri, R. Wang, Q. Zhang, G. Zhu and X. Wang, *Acta Mater.*, 2019, **175**, 222–237.
17 J.-U. Lee, D. Yoon, H. Kim, S. W. Lee and H. Cheong, *Phys. Rev. B: Condens. Matter Mater. Phys.*, 2011, **83**, 081419.
18 P. Yuan, J. Liu, R. Wang and X. J. N. Wang, *Nanoscale*, 2017, **9**, 6808–6820.
19 X. Chen and X. Wang, *J. Phys. Chem. C*, 2011, **115**, 22207–22216.
20 R. Wang, T. Wang, H. Zobeiri, P. Yuan, C. Deng, Y. Yue, S. Xu and X. J. N. Wang, *Nanoscale*, 2018, **10**, 23087–23102.
21 S. Sinha, *Ceram. Int.*, 2015, **41**, 6596–6603.
22 H. Zobeiri, R. Wang, T. Wang, H. Lin, C. Deng and X. Wang, *Int. J. Heat Mass Transfer*, 2019, **133**, 1074–1085.
23 H. Li, J. Wu, Z. Yin and H. Zhang, *Acc. Chem. Res.*, 2014, **47**, 1067–1075.
24 P. Kukura, D. Mccamant, S. Yoon, D. Wandschneider and R. J. S. Mathies, *Science*, 2005, **310**, 1006–1009.
25 D. W. McCamant, P. Kukura and R. Mathies, *Appl. Spectrosc.*, 2003, **57**, 1317–1323.
26 R. Long and O. V. Prezhdo, *Nano Lett.*, 2016, **16**, 1996–2003.
27 M. J. Shin, D. H. Kim and D. Lim, *J. Korean Phys. Soc.*, 2014, **65**, 2077–2081.
28 L. Ruan, H. Zhao, D. Li, S. Jin, S. Li, L. Gu and J. Liang, *J. Electron. Mater.*, 2016, **45**, 2926–2934.

29 H. L. Kiwia and E. F. Westrum, JR, *J. Chem. Thermodyn.*, 1975, **7**, 683–691.
30 W. Haynes, *CRC Handbook of Chemistry and Physics 92nd edition CRC Press*, Taylor and Francis, Boca Raton, 2011.
31 X. Zhang, D. Sun, Y. Li, G. H. Lee, X. Cui, D. Chenet, Y. You, T. Heinz and J. Hone, *ACS Appl. Mater. Interfaces*, 2015, 25923–25929.
32 X. Gu and R. Yang, *Appl. Phys. Lett.*, 2014, **105**, 131903.
33 A. Beal and H. Hughes, *J. Phys. C: Solid State Phys.*, 1979, **12**, 881.
34 D. Yoon, H. Moon, Y.-W. Son, J. S. Choi, B. H. Park, Y. H. Cha, Y. D. Kim and H. Cheong, *Phys. Rev. B: Condens. Matter Mater. Phys.*, 2009, **80**, 125422.
35 Y. Wang, Z. Ni, Z. Shen, H. Wang and Y. Wu, *Appl. Phys. Lett.*, 2008, **92**, 043121.
36 H.-L. Liu, C.-C. Shen, S.-H. Su, C.-L. Hsu, M.-Y. Li and L.-J. Li, *Appl. Phys. Lett.*, 2014, **105**, 201905.
37 Q. Peng, Z. Wang, B. Sa, B. Wu and Z. Sun, *Sci. Rep.*, 2016, **6**, 31994.
38 Y. Ding and B. Xiao, *RSC Adv.*, 2015, **5**, 18391–18400.
39 M. Han, J. Liu, Y. Xie and X. Wang, *Carbon*, 2017, 532–543.
40 Y. Xie, B. Zhu, J. Liu, Z. Xu and X. Wang, *Front. Energy*, 2018, **12**, 143–157.
41 N. Mingo and D. Broido, *Phys. Rev. Lett.*, 2005, **95**, 096105.
42 D. Nika, E. Pokatilov, A. Askerov and A. Balandin, *Phys. Rev. B: Condens. Matter Mater. Phys.*, 2009, **79**, 155413.